From discrete to continuous description of spherical surface charge distributions

Anže Lošdorfer Božič*

Department of Theoretical Physics, Jožef Stefan Institute, Jamova 39, SI-1000 Ljubljana, Slovenia
(Dated: November 9, 2017)

The importance of electrostatic interactions in soft matter and biological systems can often be traced to non-uniform charge effects, which are commonly described using a multipole expansion of the corresponding charge distribution. The standard approach when extracting the charge distribution of a given system is to treat the constituent charges as points. This can, however, lead to an overestimation of multipole moments of high order, such as dipole, quadrupole, and higher moments. Focusing on distributions of charges located on a spherical surface – characteristic of numerous biological macromolecules, such as globular proteins and viral capsids, as well as of inverse patchy colloids – we develop a novel way of representing spherical surface charge distributions based on the von Mises-Fisher distribution. This approach takes into account the finite spatial extension of individual charges, and leads to a simple yet powerful way of describing surface charge distributions and their multipole expansions. In this manner, we analyze charge distributions and the derived multipole moments of a number of different spherical configurations of identical charges with various degrees of symmetry. We show how the number of charges, their size, and the geometry of their configuration influence the behavior and relative importance of multipole magnitudes of different order. Importantly, we clearly demonstrate how neglecting the effect of charge size leads to an overestimation of high-order multipoles. The results of our work can be applied to construct analytical models of electrostatic interactions and multipole expansion of charged particles in diverse soft matter and biological systems.

I. INTRODUCTION

It is hard to underestimate the importance of charge and the resulting electrostatic interactions in various soft matter and biological systems. These include protein-protein and protein-polyelectrolyte interactions, viral capsid assembly and stability, interactions and crystallization of inverse patchy colloids, and drug delivery and cellular uptake of nanoparticles [1–5]. Electrostatic interactions are also highly tunable and consequently enable a controllable and tunable assembly of charged particles [2, 6]. The control over electrostatic effects can be achieved either by varying particle size and the size of their patches of charge, or by changing the properties of the surrounding electrolyte – most importantly, its salt concentration and pH value [6–13]. What is more, the charge on biological macromolecules can be in principle also regulated via induced mutations, changing the nature and charge of their amino acid composition [14].

Experimental observations and numerical simulations of electrostatic effects in these systems are often supplemented by analytical models [1–4, 15]. In a first approximation, the total charge on a particle – be it a colloid or a macromolecule – can account for a large amount of its electrostatic behavior. But while such treatment of particles as homogeneously charged is customary, non-uniform charge effects often play a significant role that cannot be neglected [16, 17]. For instance, both charge heterogeneity (patchiness) and charge fluctuation reduce the electrostatic repulsion between proteins or protein aggregates, eventually even giving way to attraction [17–21]. Likewise, heterogeneity of charge is a determining factor in the aggregation and crystallization of inverse patchy colloids, as well as in their interaction with polyelectrolytes [3, 6, 22–25]. Recent experiments have also revealed a long-range attraction between overall neutral surfaces, locally charged in a mosaic-like structure of positively and negatively charged patches [26–28].

Due to the typical size of colloidal and molecular systems, and the sheer number of atoms and charges involved in them, effective coarse-grained representations of their interaction potentials are vital for the modeling of such systems [29]. A common way of describing charge heterogeneities in particles and reducing their complexity is the multipole expansion of particles' surface charge distributions. This approach presents an efficient way of describing surface charges as continuous patches, easing the description of the rich set of surface charge patterns embedded in proteins and charged patchy particles [22, 30]. In addition to determining and classifying the electrostatic multipole moments of different proteins [10, 31, 32], multipole expansion has also been widely used to explore protein-protein, protein-ligand, and colloidal interactions [13, 22, 29, 33, 34], predict the electrophoretic mobility of proteins [35], and to provide a representation of both the protein structure [36] and of the symmetry of viral capsids [37, 38].

In obtaining a multipole representation of a particle's surface charge distribution, the charges on the particle are typically treated as point charges represented by Dirac δ functions. Similarly, the patches of charge on inverse patchy colloids are often considered to cover an exact surface area of the colloid, defined by sharp edges. While common, both descriptions are known to have multipole expansions where it is difficult to achieve an accurate representation of a surface charge distribution with

a finite number of multipole terms, due to the Dirac δ and Heaviside step functions involved [18, 39]. And while an arbitrary cutoff can in principle be chosen, e.g., by representing a surface charge distribution only by its monopole, dipole, and quadrupole moments, this leaves open the question of accuracy and relevance of high-order multipole moments.

Here, we present a novel way of constructing spherical surface charge distributions based on the von Mises-Fisher distribution, taking into account the finite extent of individual charges on a given particle. We derive the expression for the multipole moments of thusly constructed distributions, yielding a simple yet elegant form which can be used to study how the number and size of charges as well as the geometry of their configuration on a particle influences the relative relevance of multipole moments of different order. The derived model presents an improvement in the description of the multipole representation of any number of charges on a spherical particle, with a simplicity which nonetheless allows it to serve as a more accurate input for analytical models of electrostatic effects in systems of globular proteins, viral capsids, and charged patchy colloids.

II. CONSTRUCTING SPHERICAL SURFACE CHARGE DISTRIBUTIONS

We consider a point charge $q_k e_0$, located on a unit sphere of radius $R = 1$ at a position $\mathbf{r}_k = (R, \vartheta_k, \varphi_k) = (R, \Omega_k)$, written in spherical coordinates; e_0 is the elementary charge. The contribution of the point charge to the total surface charge distribution on the sphere, when written in terms of the Dirac δ function, is

$$\sigma_\delta(\Omega) = \frac{q_k e_0}{R^2} \times \delta(\Omega - \Omega_k), \qquad (1)$$

normalized so that $\int \sigma_\delta(\Omega) \, dV = q_k e_0$. Such a description, while standard, can cause difficulties when describing a contribution of many charges to the surface charge distribution and then expanding it in terms of multipoles. Specifically, the multipole coefficients of the distribution converge poorly, as an infinite sum over spherical harmonics is required to accurately represent the Dirac δ function.

In order to remedy this, we now represent a point charge $q_k e_0$ with a normal distribution on a sphere instead, writing its contribution to the total surface charge distribution as

$$\sigma_{\text{vMF}}(\Omega) = \frac{q_k e_0}{R^2} \times f(\Omega \,|\, \Omega_k, \lambda_k), \qquad (2)$$

where the function $f(\Omega \,|\, \Omega_k, \lambda)$ is the von Mises-Fisher (vMF) distribution on a unit sphere in three dimensions [40],

$$f(\Omega \,|\, \Omega_k, \lambda) = \frac{\lambda}{4\pi \sinh \lambda} \exp(\lambda \cos \gamma_k). \qquad (3)$$

Here, $\cos \gamma_k$ denotes the great-circle distance between points Ω and Ω_k on the sphere. The vMF distribution is a normal distribution on a sphere, centered around a mean direction Ω_k with a concentration parameter λ – the higher its value, the higher the concentration of the distribution around the mean direction (see Fig. 7 in Appendix A). We write the normalization factor $1/R^2$ in Eq. (2) in analogy with the spherical expression of the Dirac δ function [Eq. (1)].

Given N charges on a sphere, the total surface charge distribution can thus be written as a sum of contributions from individual charges:

$$\sigma(\Omega) = \frac{e_0}{4\pi R^2} \sum_{k=1}^{N} \frac{q_k \lambda_k}{\sinh \lambda_k} \exp(\lambda_k \cos \gamma_k), \qquad (4)$$

where each charge is represented by its own vMF distribution characterized by the mean direction Ω_k, coinciding with the position of the charge projected onto the unit sphere, and the charge's concentration parameter λ_k, describing its spatial extension around the mean position. The surface charge distribution, Eq. (4), can in turn be expanded in terms of its multipole moments

$$\sigma(\Omega) = \frac{e_0}{4\pi R^2} \sum_{l,m} \sigma_{lm} Y_{lm}(\Omega). \qquad (5)$$

A lengthy derivation, given in Appendix B, yields a very elegant expression for the multipole coefficients σ_{lm},

$$\sigma_{lm} = 4\pi \sum_k q_k \, g_l(\lambda_k) \, Y_{lm}^*(\Omega_k), \qquad (6)$$

where we have defined

$$g_l(\lambda) = \frac{\lambda}{\sinh \lambda} \, i_l(\lambda). \qquad (7)$$

Here, $i_l(x)$ are the modified spherical Bessel functions of the first kind [41]. Rather unexpectedly, the multipole coefficients are determined by a single function dependent on the multipole order ℓ and the concentration parameter λ_k. With the knowledge of multipole coefficients [Eq. (6)], we can now also insert them back into Eq. (4) to obtain the total surface charge distribution.

Given an expansion of a surface charge distribution in terms of its multipole coefficients, we define the multipole magnitude S_l of order ℓ as

$$S_l = \sqrt{\frac{4\pi}{2l+1} \sum_m |\sigma_{lm}|^2}. \qquad (8)$$

Inserting the expression for the multipole coefficients, Eq. (6), we obtain the normalized multipole magnitudes (Appendix C)

$$\frac{S_l}{|S_0|} = \left(\sum_k |q_k| \right)^{-1} \left[\sum_{k=t} q_k^2 \, g_l^2(\lambda_k) + 2 \sum_{k>t} q_k q_t \, g_l(\lambda_k) \, g_l(\lambda_t) \, P_l(\cos\gamma_{kt}) \right]^{1/2}. \tag{9}$$

The monopole moment S_0 relates of course to the total charge Q, whereas the multipole moments of the first and second order correspond to the dipole and quadrupole moment, respectively, and can be easily related to their Cartesian forms [10]. In order to enable an easy comparison between configurations with the same number of charges but different total charge, we have normalized the multipole magnitudes in Eq. (9) with the absolute value of the monopole moment, $|S_0| = 4\pi \sum_k |q_k| = 4\pi|Q|$.

We have thus derived the multipole coefficients for an arbitrary distribution of N charges on a unit sphere [Eq. (6)], where we have assigned to them vMF distributions with given mean directions Ω_k and concentration parameters λ_k. Through this, we have obtained a very simple expression both for the resulting total surface charge distribution and its corresponding multipole moments [Eq. (9)]. Such an approach ascribes a finite, continuous spatial extent to each charge, providing a more realistic description and at the same time avoiding the difficulties related to the multipole expansion of Dirac δ functions.

A. Configurations of identical charges

In order now to explore the consequences of the derived expressions for the surface charge distribution and its multipole moments, we will limit ourselves in the rest of the paper to configurations where all the charges possess identical properties, $q_k = q = 1$ and $\lambda_k = \lambda$.

Such an assumption immediately enables us to study certain limiting cases of our results (Appendix D): When the concentration parameter λ tends to 0, the surface charge distribution of any configuration of charges expectedly becomes a uniform distribution on the sphere, described by its total charge. On the other hand, when λ tends to infinity, the surface charge distribution reduces to a sum over Dirac δ functions of individual charges [Eq. (1)].

More interestingly, the multipole magnitudes of a configuration of N identical charges can be expressed as

$$\frac{S_l}{|S_0|} = g_l(\lambda) \times \left(\frac{1}{N} + \frac{2}{N^2} \sum_{k>t} P_l(\cos\gamma_{kt}) \right)^{1/2} \tag{10}$$

$$= g_l(\lambda) \times \frac{S_l^\infty}{|S_0|}. \tag{11}$$

From here, we see that there are two major factors determining the relative contribution of a given multipole moment S_l to the surface charge distribution. The first factor is given by the function $g_l(\lambda)$, and the second by the geometry of the configuration of the N charges, given

by their spherical distances $\cos\gamma_{kt}$. The latter are indeed all that determines the multipole magnitudes in the limit $\lambda \to \infty$, as $\lim_{\lambda\to\infty} g_l(\lambda) = 1 \ \forall l$. On the other hand, when $\lambda \to 0$, we have $\lim_{\lambda\to 0} g_l(\lambda) \propto \lambda^l$ and the low-order multipoles become increasingly dominant. A more detailed discussion of the different limiting cases is given in Appendix D.

III. RANDOM CONFIGURATIONS OF IDENTICAL CHARGES AND THE ROLE OF SYMMETRY

We study the implications of our results by applying them to different configurations of N identical charges on a unit sphere and analyzing the properties of the resulting surface charge distributions. All the charges share the same properties, $q_k = q = 1$ and $\lambda_k = \lambda$, with λ and N being variable. For comparison, we use three different types of charge configurations on a sphere:

(i) Random distributions of charges, where the positions of charges are distributed uniformly on the sphere.

(ii) Distributions of charges with some minimal distance between them. The positions of these charges are generated randomly and picked according to Mitchell's best-candidate algorithm [42] (approximating Poisson disc sampling and blue noise). In this manner, we prevent charges from being distributed too closely together, as can, for instance, happen in scheme (i). The resulting positions of charges are, while random, no longer independent.

(iii) Distributions of charges based on the solutions of the Thomson problem, which minimizes the electrostatic energy of such a configuration [43]. Compared to schemes (i) and (ii), the charges in these configurations are spaced the furthest apart, and the configurations exhibit various symmetries, including tetrahedral, octahedral, and icosahedral (depending on the number of charges N).

We will refer to these configurations as random, Mitchell, and Thomson configurations, respectively. While the solutions of the Thomson problem, (iii), provide unique configurations for a given N, generating them randomly – either uniformly, (i), or with Mitchell's algorithm, (ii) – can yield many different configurations. In the latter two cases we thus generate, for each N, $M = 5000$ different configurations, allowing us to operate in terms of average quantities, where the average is taken over all M configurations.
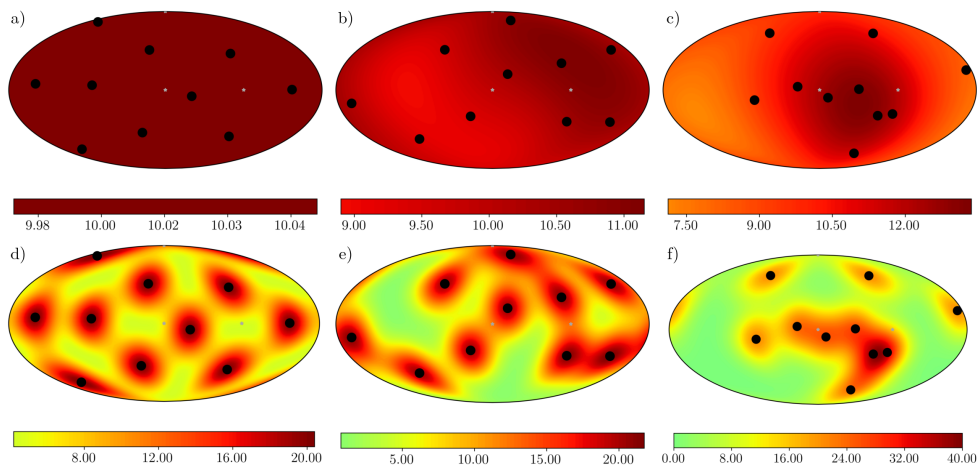
Figure 1. Surface charge distributions for configurations of $N = 10$ identical charges on a unit sphere. The distributions are mapped from a sphere onto a plane using Mollweide projection. **(a)**, **(d)** Configuration based on the solution of the Thomson problem; **(b)**, **(e)** configuration with charge positions generated using Mitchell's best candidate algorithm; **(c)**, **(f)** configuration generated by uniformly random positioning of charges. The value of the concentration parameter in panels **(a)**-**(c)** is $\lambda = 1$, and in panels **(d)**-**(f)** $\lambda = 10$. The color scheme shows the angular variation of the surface charge distribution in arbitrary units, with warmer colors indicating larger values.

In Fig. 1, we use the three different schemes *(i)-(iii)* to obtain configurations of $N = 10$ identical charges and their surface charge distributions, which have been projected from a sphere onto a plane using Mollweide projection [44]. In addition, the configurations are shown at two different values of the concentration parameter, $\lambda = 1$ and $\lambda = 10$ (cf. also Fig. 7 in Appendix A). We see that, for small λ, the Thomson configuration is almost indistinguishable from a uniform charge distribution. Random and Mitchell configurations show more variation, especially if the charges are allowed to be located close to each other. At higher λ, where the influence of charges is more concentrated around their positions, the deviations from a uniform distribution become more prominent in all three configurations. Again, however, the relative positions of the charges determine the extent of this variation. These observations indicate that indeed λ and the relative positions of the charges (given by $\cos \gamma_{kt}$) will determine the multipole characterization of a given configuration of charges. Mitchell's algorithm, *(ii)*, positions the charges so that there is a minimal distance between them, leading to a "layered" distribution of distances between charges; on the other hand, random positioning of charges onto the sphere, *(i)*, tends to distribute them uniformly on average (see Fig. 8 in Appendix E). Lastly, Thomson configurations exhibit the largest distances between particles and the highest overall symmetry.

A. Multipole expansion

Figure 1 provides us with an insight into how a particular configuration of charges and their concentration parameter λ influence the resulting surface charge distribution. However, as it is difficult to assess the general influence of the number of charges and their properties based on their surface charge distribution alone, we now turn our attention to their multipole magnitudes [Eq. (11)].

Figure 2 shows the distributions of the first 6 normalized multipole moments for 5000 different random and Mitchell configurations of $N = 10$ identical charges. We can see that, in both cases, at small values of λ the multipole moments of high order ℓ are quickly suppressed, and the surface charge distribution is thus dominated by its monopole moment. When λ increases, the high-order multipoles drop off ever more slowly until they become comparable among each other in the limit $\lambda \to \infty$. On average, random configurations tend to have much larger low-order multipoles (dipole, quadrupole) compared to Mitchell configurations with a minimum distance between the charges; this difference disappears for high-order multipoles. All these observations stem from the mean values of multipoles obtained by averaging over the 5000 different configurations; within these, there is still a significant amount of variation, especially for low ℓ.

As the concentration parameter λ is increased, multipoles of high order become less and less negligible (Fig. 2). This behavior becomes even more pronounced when we plot the normalized total power of order ℓ, $P_l/|P_0|$, obtained by terminating the expression for total power [Eq. (C4)] at a given ℓ. The total power consists of a sum of squared multipole magnitudes, and is shown in Fig. 3 for configurations of $N = 10$ identical charges. Again, we can see clearly that at low λ, the surface charge distribution of any configuration is dominated by its monopole moment. Upon a gradual increase in λ, the next few multipole moments become more im-
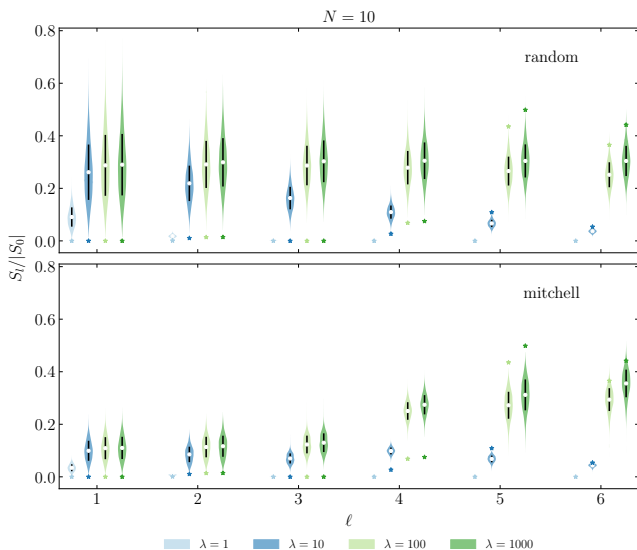
Figure 2. Violin plot of the first 6 multipole magnitudes for random and Mitchell configurations of $N = 10$ identical charges. Each entry in the violin plot shows a (mirrored) distribution of normalized magnitudes of 5000 different configurations, with the central symbols denoting the mean and the bars denoting the corresponding standard deviation. Star symbols show the multipole magnitudes of the corresponding Thomson configuration. The plot is shown for four different values of the concentration parameter λ.
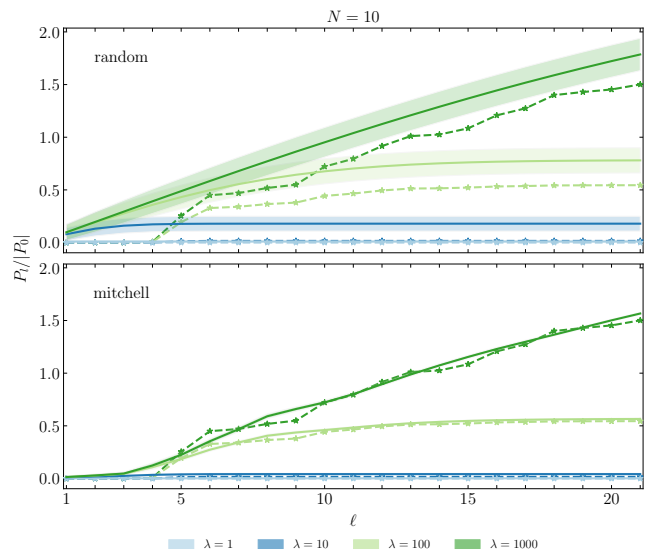
Figure 3. Normalized total power $P_l/|P_0|$ of random and Mitchell configurations of $N = 10$ identical charges, obtained by summing the squares of multipole magnitudes up to order ℓ. Full lines show the mean values, obtained by averaging over 5000 different configurations, while the shaded regions denote the corresponding standard deviations. The latter are negligible for Mitchell configurations. Dashed lines and star symbols show the total power for the corresponding Thomson configuration. The plot is shown for four different values of the concentration parameter λ.

portant, while the majority of the multipoles still do not contribute to the total power. However, with a still further increase in λ, more and more multipoles need to be summed before the total power converges, and when $\lambda = 1000$, we are far from convergence even when we truncate the sum only at $\ell = 21$. This observation holds regardless of which of the three configuration schemes *(i)*-*(iii)* we choose. We can also observe that the total power of Mitchell configurations of charges, keeping a minimum distance between them, matches quite closely the total power of the corresponding Thomson configuration, while the total power of random configurations is always higher, especially due to the higher values of dipole and quadrupole moments.

Figures 9 and 10 in Appendix E show the results for configurations of $N = 20$ identical charges, analogous to those presented in Figs. 2 and 3 for configurations of $N = 10$ charges. We can see that the general behavior is similar in the two cases. Notably, though, a higher number of charges lowers the overall magnitudes of multipoles compared to the monopole moment, and in case of Mitchell configurations, the first non-negligible multipole occurs at a later value of ℓ compared to the case of $N = 10$ charges ($\ell \sim 8$ and $\ell \sim 6$, respectively).

The first non-negligible multipole in an expansion of a surface charge distribution thus appears to be in large part determined by any symmetry a given configuration might possess. Thomson configuration of $N = 10$ identical charges possesses a D_{4d} symmetry [43], and

as such, its first non-vanishing multipole should be the quadrupole, $\ell = 2$ [45]. From Fig. 4 we can observe that this is indeed the case. Multipole magnitudes reach a first peak, however, at $\ell = 5$ and $\ell = 6$. Compared with the corresponding random and Mitchell configurations, the Thomson configuration also shows the most variation between multipoles of different order – that is, while some multipoles are strongly represented in the expansion, others are completely absent; this is especially noticeable in the limit $\lambda \to \infty$, where the only contribution to the multipoles is due to the geometry of the configuration [Eq. (11)]. We can see that the higher the order of the multipole, ℓ, the more slowly this limiting value is reached.

The results for configurations of $N = 10$ identical charges indicate that the multipole description of a surface charge distribution and its deviations from a uniform distribution are influenced by several factors (Fig. 4). In configurations where high-order multipoles (large ℓ) are dominant, the description of charges will approach the limit of Dirac δ functions ($\lambda \to \infty$) slowly, i.e., their surface charge distribution will be approximated well by a uniform distribution in a wider range of λs. Another factor influencing the deviation from a uniform distribution is the limiting value of the multipole magnitudes, S_l^∞, dependent solely on the geometrical distribution of the charges. A lower limiting value, typical of completely random distributions, implies that, in spite of
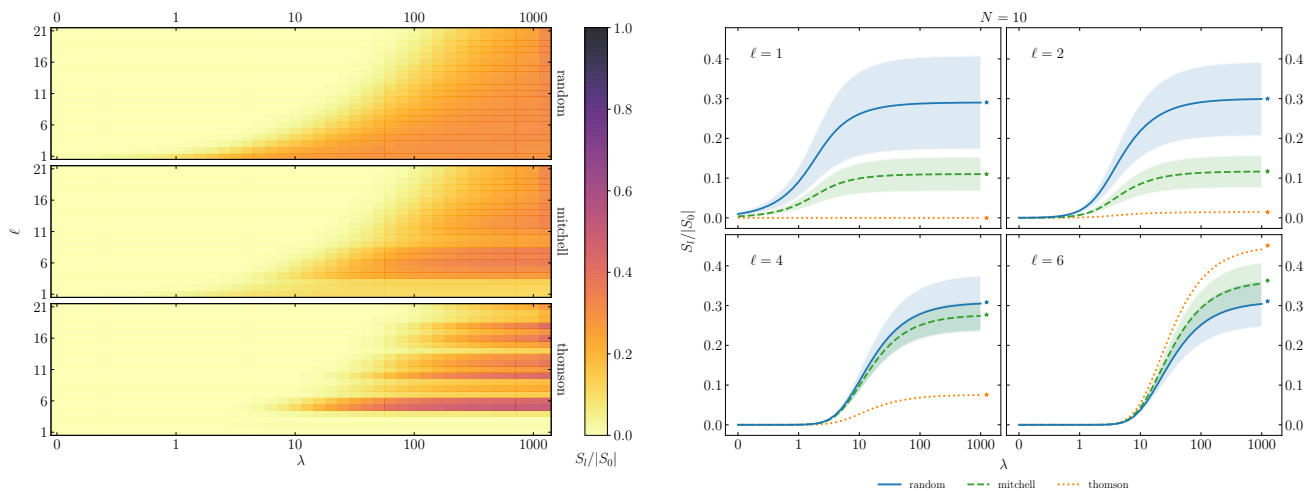
Figure 4. Heatmap of normalized multipole magnitudes $S_l/|S_0|$ as a function of λ and ℓ for different configurations of $N = 10$ identical charges. Plots isolate the λ-dependence of multipoles with order $\ell = 1, 2, 4$, and 6. In the case of random and Mitchell configurations, the heatmap and the full lines in the plots show the mean values obtained by averaging over 5000 different configurations, while the shaded regions denote the corresponding standard deviations. The last column of the heatmap and the star symbols in the plots show the values of multipole magnitudes in the limit $\lambda \to \infty$, $S_l^\infty/|S_0|$.

how quickly this limit is attained with λ, the uniform distribution given by the monopole moment will remain dominant.

We now wish to generalize these observations to configurations with an arbitrary number of charges. In order to do that, we will characterize the behavior of multipole magnitudes S_l with two parameters: first, with their limiting value S_l^∞, and second, with the value of the concentration parameter where a multipole magnitude reaches 10% of the monopole moment, which we will denote $\lambda_{0.1}$:

$$\left.\frac{S_l}{|S_0|}\right|_{\lambda_{0.1}} = g_l(\lambda_{0.1}) \times \frac{S_l^\infty}{|S_0|} = 0.1. \qquad (12)$$

The dependence of these two parameters on the number of identical charges in a configuration, N, is shown in Figs. 5 and 6 for a large number of multipole magnitudes. First of all, we see that, for random configurations of charges, the limiting value S_l^∞ changes only slowly with ℓ, while it decreases with N (Fig. 5). However, the value of ℓ influences rather strongly the parameter $\lambda_{0.1}$ – the speed at which the limiting value S_l^∞ is attained (Fig. 6). In contrast, $\lambda_{0.1}$ is not influenced much by the number of charges in a random configuration.

The number of charges N has a much bigger influence on the behavior of Thomson configurations. Partially, this is to be expected, as they exhibit various symmetries at different N, resulting in a strong presence of multipoles of given ℓ and on the almost complete vanishing of other multipoles. For instance, it is known that for configurations with tetrahedral, octahedral, and icosahedral symmetries, only certain values of ℓ are permitted in the multipole expansion of the surface charge distribution [18, 37]: $\ell_{\text{tet}} = 4i + 6j\,(+3)$, $\ell_{\text{oct}} = 4i + 6j\,(+9)$, and $\ell_{\text{ico}} = 6i + 10j\,(+15)$; configurations with odd val-
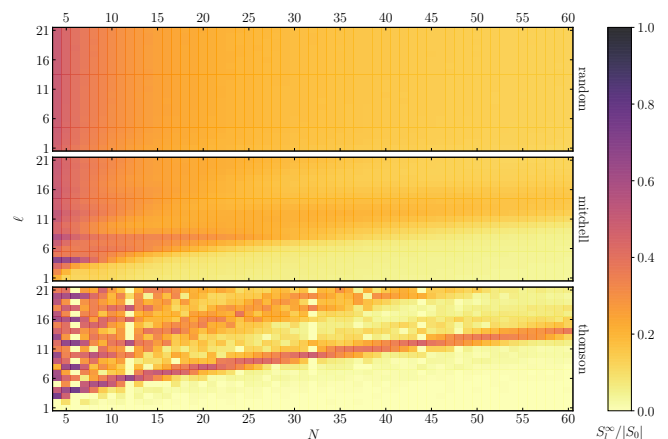

Figure 5. Heatmap showing the limiting value of the multipole magnitudes $S_l^\infty/|S_0|$ as a function of N and ℓ. The value of $S_l^\infty/|S_0|$ is obtained in the limit $\lambda \to \infty$, and depends solely on the distances between charges in a given configuration. In the case of random and Mitchell configurations, the heatmap shows the mean values obtained by averaging over 5000 different configurations.

ues of ℓ are those which lack inversion symmetry. The symmetries of different configurations and the permitted multipoles in their expansion are reflected in a checkered pattern in the heatmaps in Figs. 5 and 6, a pattern which is completely absent in the case of random configurations.

In addition to this, Thomson configurations exhibit vanishing multipole moments of low order ℓ, the amount of which increases with increasing N. For example, while the dipole and quadrupole moment are negligible for a Thomson configuration with $N = 10$ charges, all of the
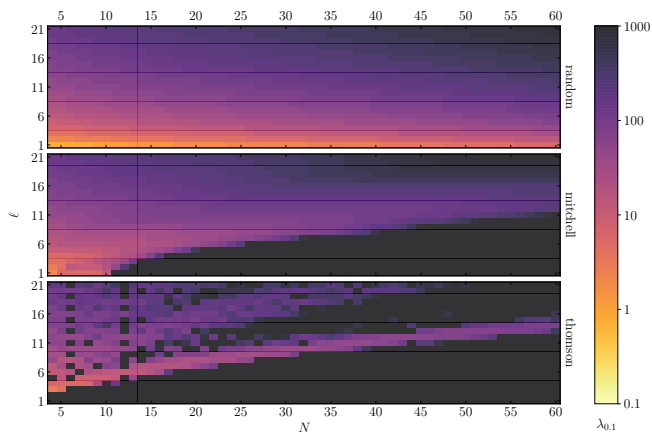
Figure 6. Heatmap showing the value of the concentration parameter where a multipole magnitude reaches 10% of the monopole magnitude (total charge), $\lambda_{0.1}$, as a function of N and ℓ. A value of $\lambda_{0.1} = 1000$ indicates that a multipole does not reach the 10% value of the monopole in the considered range of λs. In the case of random and Mitchell configurations, the heatmap shows the mean values obtained by averaging over 5000 different configurations.

first 10 multipole moments are negligible for a Thomson configuration with $N = 60$ charges. What is more, these vanishing multipole moments appear to occur periodically in "islands" of ℓ numbers, the extent of which increases with N (see also Fig. 11 in Appendix E).

Mitchell configurations present a middle ground between random and Thomson configurations. The variation of S_l^∞ and $\lambda_{0.1}$ occurs gradually with N, in a similar fashion to random configurations, yet at the same time we can observe the same vanishing multipoles of low order at higher numbers of charges as we saw for Thomson configurations. Individual multipoles also tend to be more pronounced in Mitchell configurations compared to the multipoles of random configurations, yet not so strikingly as in the symmetric Thomson configurations.

Taken together, our results for configurations of identical charges show that the multipole magnitudes of their surface charge distributions depend strongly on the exact geometry of the configuration, with clear differences between randomly positioned charges, configurations where charges are placed a minimum distance apart, and configurations of very high symmetry. In addition, both the number of charges and their size – given by the concentration parameter – place the surface charge distribution of a configuration of charges in different regimes, where the distribution can either behave solely as a uniform distribution, or needs a large number of high-order multipoles to be accurately represented.

IV. DISCUSSION AND CONCLUSIONS

In this work, we have presented a novel way of constructing continuous surface charge distributions of

spherical particles composed of numerous charges. Our approach is based on the description of individual charges with a vMF distribution on a sphere, taking into account the finite extent of the charges. With this, we were able to extract the electrostatic multipoles of such surface charge distributions and analyze their behavior as a function of the multipole order ℓ, and the number N and size (concentration parameter λ) of the charges. Analytically, we have derived the precise relation of the multipole magnitudes to the size of the charges and the geometry of their configuration on the sphere. We have explored the predictions of our approach on different configurations of identical charges, generated either randomly or by using Mitchell's algorithm, or extracted from the solutions of the Thomson problem.

While we have considered configurations of charges with identical properties, the results derived in this paper allow an easy generalization to arbitrary configurations of fractional charges q_k with concentration parameters λ_k (which take into account their relative extension on a unit sphere with $R = 1$). In addition, given a "physical" size of a charge a_k, we can rewrite the concentration parameter for an arbitrary size of the sphere R as

$$\lambda_k = \frac{R}{a_k}. \tag{13}$$

This implies that, for a given size of a charge, the parameter λ will be larger for larger spheres, where the same charge will appear more localized on a larger than on a smaller sphere. In this way, our approach can be used to study the surface charge distributions on biomolecules of different sizes, ranging from small globular proteins ($R \gtrsim 1$ nm) to larger viral capsids ($R \gtrsim 10$-20 nm) [10, 46], thus spanning a range of $\lambda_k \gtrsim 1$-100, depending on the size of the macromolecule in question. This of course makes it necessary to be able to estimate the value of the parameter a_k, which can be obtained from the biochemical nature of the molecules (such as different amino acids) carrying the charge in a given system.

An important conclusion we can draw from our results is that the relationship between the size of the charges relative to the size of the sphere they are located on plays a significant role in determining the resulting surface charge distributions. We have seen that going from very spread-out charges (small λ) to charges that can be treated as Dirac δ functions (large λ) results in a wildly different relative importance of the corresponding multipole magnitudes. Specifically, a surface charge distribution constructed out of point charges will need in principle an infinite sum of multipoles in order to be represented accurately, potentially masking the importance of low-order multipoles. Consequently, such a description could lead to an over- or underestimation of dipole and quadrupole moments. Our results also indicate that even in descriptions of general charge distributions of molecules, taking into account the finite extension of charges could have a pronounced effect on the

determination of their electrostatic multipoles [47, 48].

In general, our approach also helps distinguish the regime where a given configuration of charges on a sphere can be described well by a uniform distribution from the regime where the charges are localized enough that their geometry and symmetry determine the largest multipoles in the expansion of the surface charge distribution. While the geometry of a particular configuration of charges turns out to play a large role, it will nonetheless tend to a uniform distribution when $\lambda \ll 1$, whereas the multipole magnitudes will be determined solely by the geometry of the configuration when $\lambda \gg 1$. In the intermediate regime of λs, increasing the number of charges in a configuration will in general reduce the importance of high-order multipoles, the more so the less symmetric the configuration. At the same time, multipoles of low order are prominent at small values of λ, and the high-order multipoles become comparable only when λ is increased.

The parameter space of biological macromolecules and colloids can in fact span a large range of values studied in this work. The charge of both small globular proteins and large capsid assemblies is carried by the same amino acids, meaning that the concentration parameters of charges will be smaller for the globular proteins than for viral capsids. On the other hand, viral capsids can carry several hundreds or thousands of individual charges, while the smaller proteins are often composed of only a few tens of charges. Consequently, we can expect a large variation in the multipole behavior of the surface charge distributions in different systems.

A particular observation that should be of importance when describing the surface charge distributions in viral capsids is that the order ℓ of the dominant multipole in symmetric distributions increases with an increasing number of charges in a configuration. This is in contrast to random configurations of charges, which tend to be dominated by low-order multipoles, no matter the number of charges. As viral capsids possess very high symmetry – typically icosahedral – our approach can be used to extract the dominant multipole describing the symmetry of a particular configuration, which was recently shown to play a role in orientational phase transitions in capsids [49].

The approach presented in this work enables a simple yet powerful construction of continuous surface charge distributions from individual charges on spherical particles, taking into account the finite size of each charge. This allows for a construction of various analytical models based on multipole expansion that can be used in describing systems of inverse patchy colloids, small globular proteins, and viral capsids of different sizes. In addition, the approach presented here can help elucidate the relative relevance of multipole magnitudes in a given system, and can help distinguish the cases where total charge provides a sufficient description of the electrostatic properties from the cases where a more detailed multipole expansion is needed.

Appendix A: von Mises-Fisher distribution

Von Mises-Fisher (vMF) distribution is a normal probability distribution on the $(p-1)$-dimensional sphere in $\mathcal{R}^p$ [40]. The vMF distribution for a random p-dimensional vector $\mathbf{r}$ is given by

$$f_p(\mathbf{r} \,|\, \mathbf{r}_0, \lambda) = C_p(\lambda) \exp(\lambda \, \mathbf{r}_0^T \mathbf{r}). \tag{A1}$$

Here, $\lambda \geqslant 0$, $|\mathbf{r_0}| = 1$, and the normalization constant C_p is equal to

$$C_p(\lambda) = \frac{\lambda^{p/2-1}}{(2\pi)^{p/2} I_{p/2-1}(\lambda)}, \tag{A2}$$

where I_ν denotes the modified Bessel functions of the first kind [41]. vMF distribution is a normal distribution on a sphere, where the parameter $\mathbf{r}_0$ is the mean direction of the distribution, and the parameter λ is the concentration parameter – the higher its value, the higher the concentration of the distribution around the mean direction. A generalization of the vMF distribution to a bivariate normal distribution with an unconstrained covariance matrix is called the spherical Fisher-Bingham or Kent distribution [50].

In three dimensions – on a unit sphere $\mathcal{S}_2$ – the normalization constant of the vMF distribution reduces to

$$C_3 = \frac{\lambda}{4\pi \sinh \lambda} = \frac{\lambda}{4\pi(e^\lambda - e^{-\lambda})}, \tag{A3}$$

and we can thus write

$$f_3(\mathbf{r} \,|\, \mathbf{r}_0, \lambda) = \frac{\lambda}{4\pi \sinh \lambda} \exp(\lambda \, \mathbf{r}_0^T \mathbf{r}). \tag{A4}$$

Since any vector on the unit sphere can be represented in spherical coordinates as

$$\mathbf{r} = (\cos\varphi \sin\vartheta, \sin\varphi \sin\vartheta, \cos\vartheta). \tag{A5}$$

the exponent of the vMF distribution becomes

$$\exp(\lambda \, \mathbf{r}_0^T \mathbf{r}) = \exp(\lambda \cos\gamma_0), \tag{A6}$$

where γ_0 denotes the great-circle distance between points Ω and Ω_0,

$$\cos\gamma_0 = \cos\vartheta \cos\vartheta_0 + \cos(\varphi - \varphi_0) \sin\vartheta \sin\vartheta_0. \tag{A7}$$

With this, we can write the vMF distribution on a unit sphere centered around a point Ω_0 as

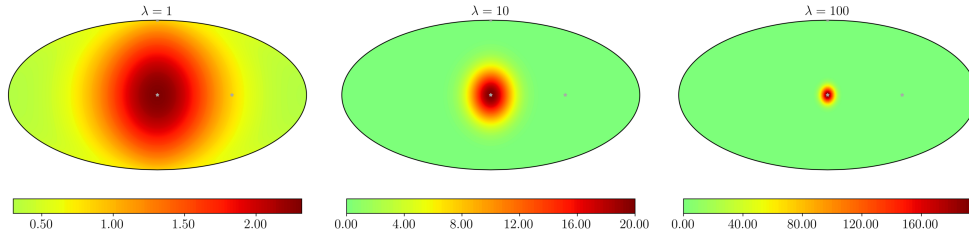$$f_3(\Omega \,|\, \Omega_0, \lambda) = \frac{\lambda}{4\pi \sinh \lambda} \exp(\lambda \cos\gamma_0). \tag{A8}$$

Figure 7. Distribution of a single point charge with $q = 1$ located on the x axis on a unit sphere. The distribution is shown for three different values of $\lambda = 1, 10, 100$. The distribution was mapped from a sphere to a plane using Mollweide projection, and the coordinate axes are shown with gray stars.

The distribution is normalized so that

$$\oint_{\mathcal{S}_2} \mathrm{d}\Omega \, f_3(\Omega \,|\, \Omega_0, \lambda) = 1. \tag{A9}$$

The parameter λ determines the concentration of the distribution centered around Ω_0. For $\lambda = 0$, the distribution is uniform on the sphere, while for $\lambda \to \infty$, the distribution tends to a Dirac δ function. Applying this to a distribution of a single point charge on a unit sphere [Eq. (1)], Fig. 7 shows the distribution of a charge with $q = 1$ located on the x-axis, for three different values of λ. When the concentration parameter is small, $\lambda = 1$, the distribution extends across most of the unit sphere; however, with increasing λ, the influence of the charge becomes more and more localized.

Appendix B: Derivation of multipole coefficients of the vMF surface charge distribution

We start with the vMF surface charge distribution of a number of point charges q_k with concentration parameters λ_k and centered on positions Ω_k [Eq. (4)]. From the corresponding multipole expansion, Eq. (5), we obtain for the multipole coefficients

$$\sigma_{lm} = \sum_k \frac{q_k \lambda_k}{\sinh \lambda_k} \oint \mathrm{d}\Omega \, Y_{lm}^*(\Omega) \, \exp(\lambda_k \cos \gamma_k). \tag{B1}$$

The exponential function can be written as a power series, wherefrom we get

$$\sigma_{lm} = \sum_k \frac{q_k \lambda_k}{\sinh \lambda_k} \sum_n \frac{\lambda_k^n}{n!} \oint \mathrm{d}\Omega \, Y_{lm}^*(\Omega) \, \cos^n \gamma_k. \tag{B2}$$

Introducing $x_k = \cos \gamma_k$, we split the sum over n into even and odd terms:

$$\sigma_{lm} = \sum_k \frac{q_k \lambda_k}{\sinh \lambda_k} \left\{ \oint \mathrm{d}\Omega \, Y_{lm}^*(\Omega) \sum_n \frac{\lambda_k^{2n}}{(2n)!} x_k^{2n} \right.$$
$$\left. + \oint \mathrm{d}\Omega \, Y_{lm}^*(\Omega) \sum_n \frac{\lambda_k^{2n+1}}{(2n+1)!} x_k^{2n+1} \right\}. \tag{B3}$$

Based on Ref. [51], we postulate that

$$\sum_{n=0}^{\infty} \alpha_n x_k^n = \sum_{m=0}^{\infty} a_m P_m(x_k), \tag{B4}$$

where $P_n(x)$ are the Legendre polynomials, and the sum runs either over $m = n = $ even or $m = n = $ odd. Using the orthogonality of spherical harmonics, we can write

$$\sum_n \alpha_n \int_{-1}^1 x^n P_m(x) \mathrm{d}x = \frac{2}{2m+1} a_m. \tag{B5}$$

The integral can be split in two parts, and taking into account $P_m(-x) = (-1)^m P_m(x)$, we see that

$$a_m = \frac{2m+1}{2} \sum_n \alpha_n \times \begin{cases} 2 \int_0^1 x^n P_m(x) \mathrm{d}x & , \quad n+m \text{ even} \\ 0 & , \quad n+m \text{ odd} \end{cases} \quad , \tag{B6}$$

and the integral can be expressed in terms of Γ functions [41]:

$$\int_0^1 x^n P_m(x) \mathrm{d}x = \frac{\sqrt{\pi} \, 2^{-n-1} \Gamma(1+n)}{\Gamma(1+n/2 - m/2)\Gamma(3/2 + n/2 + m/2)}. \tag{B7}$$

By writing $a_m = \sum_n A_{mn} \alpha_n$, we get from Eq. (B6)

$$A_{mn} = \frac{\sqrt{\pi} \, 2^{-n-1} (2m+1)\Gamma(1+n)}{\Gamma(1+n/2-m/2)\Gamma(3/2+n/2+m/2)} \quad , \quad n+m \text{ even}; \quad m \leqslant n, \tag{B8}$$

and 0 otherwise. We immediately see that when $n = $ even, so is m, and conversely, when $n = $ odd, so is again m. Summing over even powers of x in Eq. (B4) will thus yield only $P_n(x)$ of even order, and similarly for the sum over odd powers. In addition, the coefficients A_{mn} are nonzero only when $m \leqslant n$. From Eq. (B3) we have $\alpha_n = \lambda^n/n!$, and so it follows that

$$a_m = \sum_{n \geqslant m}^{\infty} A_{mn} \frac{\lambda^n}{n!} = \sum_{n \geqslant m}^{\infty} \frac{\lambda^n \sqrt{\pi}\, 2^{-n-1}\, (2m+1)}{\Gamma(1 + n/2 - m/2)\, \Gamma(3/2 + n/2 + m/2)} \quad , \quad n + m \text{ even.} \tag{B9}$$

Inserting now the theorem in Eq. (B4) into Eq. (B3), we obtain

$$\sigma_{lm} = \sum_k \frac{q_k \lambda_k}{\sinh \lambda_k} \left\{ \oint d\Omega\, Y_{lm}^*(\Omega) \sum_s a_{2s} P_{2s}(x_k) + \oint d\Omega\, Y_{lm}^*(\Omega) \sum_s a_{2s+1} P_{2s+1}(x_k) \right\}. \tag{B10}$$

Next, we use the addition theorem for the spherical harmonics to write

$$\sigma_{lm} = \sum_k \frac{q_k \lambda_k}{\sinh \lambda_k} \left\{ \sum_s a_{2s} \oint d\Omega\, Y_{lm}^*(\Omega) \frac{4\pi}{2(2s)+1} \sum_{t=-2s}^{2s} Y_{2s,t}(\Omega)\, Y_{2s,t}^*(\Omega_k) + \right.$$
$$\left. \sum_s a_{2s+1} \oint d\Omega\, Y_{lm}^*(\Omega) \frac{4\pi}{2(2s+1)+1} \sum_{t=-2s+1}^{2s+1} Y_{2s+1,t}(\Omega)\, Y_{2s+1,t}^*(\Omega_k) \right\}. \tag{B11}$$

Rearranging the order of summation and integration, the integrals evaluate into Dirac δ functions. By virtue of this, the sums over s and t disappear, yielding

$$\sigma_{lm} = \sum_k \frac{q_k \lambda_k}{\sinh \lambda_k} \times \begin{cases} a_l \dfrac{4\pi}{2l+1} Y_{l,m}^*(\Omega_k) & , \quad l \text{ even} \\[2ex] a_l \dfrac{4\pi}{2l+1} Y_{l,m}^*(\Omega_k) & , \quad l \text{ odd} \end{cases}. \tag{B12}$$

Using the expression for the coefficients a_m in Eq. (B9), we obtain from Eq. (B12):

$$\sigma_{lm} = 4\pi \sum_k q_k Y_{lm}^*(\Omega_k) \sum_{s \geqslant l}^{\infty} \frac{\lambda_k^{s+1}}{\sinh \lambda_k} \frac{\sqrt{\pi}\, 2^{-s-1}}{\Gamma(s/2 - l/2 + 1)\, \Gamma(s/2 + l/2 + 3/2)} \quad , \quad l + s \text{ even,} \tag{B13}$$

which holds true for both even and odd l. Introducing

$$g_l(\lambda) = \sum_{s \geqslant l}^{\infty} \frac{\lambda^{s+1}}{\sinh \lambda} \frac{\sqrt{\pi}\, 2^{-s-1}}{\Gamma(s/2 - l/2 + 1)\, \Gamma(s/2 + l/2 + 3/2)} \quad , \quad l + s \text{ even,} \tag{B14}$$

we can write the multipole coefficients as

$$\sigma_{lm} = 4\pi \sum_k q_k\, g_l(\lambda_k)\, Y_{lm}^*(\Omega_k). \tag{B15}$$

What is more, using Mathematica software [52] we can show that the function $g_l(\lambda)$ evaluates to

$$g_l(\lambda) = \frac{\lambda}{\sinh \lambda}\, i_l(\lambda), \tag{B16}$$

where

$$i_l(x) = \sqrt{\frac{\pi}{2x}}\, I_{l+1/2}(x) \tag{B17}$$

are the modified spherical Bessel functions of the first kind [41]. Thus, we finally obtain the result of Eq. (6).

Appendix C: Multipole magnitudes, total power, and bond order parameters

In order to obtain the multipole magnitudes from Eq. (8), we insert the expression for the multipole coefficients, Eq. (6), into the squared form of the magnitudes. Thus, we get

$$S_l^2 = \frac{(4\pi)^3}{2l+1} \sum_m \left[\left(\sum_k q_k\, g_l(\lambda_k)\, Y_{lm}^*(\Omega_k) \right) \times \left(\sum_t q_t\, g_l(\lambda_t)\, Y_{lm}(\Omega_t) \right) \right]. \tag{C1}$$

Using the addition theorem for spherical harmonics, we then obtain

$$S_l^2 = (4\pi)^2 \sum_{k,t} q_k q_t g_l(\lambda_k) g_l(\lambda_t) P_l(\cos\gamma_{kt}). \quad \text{(C2)}$$

Taking into account that $P_l(\cos\gamma_{kk} = 1) = 1$ and that $\cos\gamma_{kt} = \cos\gamma_{tk}$, this expression simplifies to

$$S_l^2 = (4\pi)^2 \left[\sum_{k=t} q_k^2 g_l^2(\lambda_k) \right.$$
$$\left. + 2\sum_{k>t} q_k q_t g_l(\lambda_k) g_l(\lambda_t) P_l(\cos\gamma_{kt}) \right]. \quad \text{(C3)}$$

Normalizing this expression with $|S_0| = 4\pi \sum_k |q_k|$, we obtain Eq. 9. Knowing the multipole magnitudes, we can also immediately write down the total power

$$P = \int_\Omega |\sigma(\Omega)|^2 \mathrm{d}\Omega = \sum_l \frac{4\pi}{2l+1} \sum_m |\sigma_{lm}|^2 = \sum_l S_l^2. \quad \text{(C4)}$$

Appendix D: Limiting cases

In the limit where $\lambda \to 0$, the asymptotic behavior of $g_l(\lambda)$ is given by

$$\lim_{\lambda\to 0} g_l(\lambda) \propto \lambda^l + \mathcal{O}(\lambda^{l+2}), \quad \text{(D1)}$$

and specifically, $\lim_{\lambda\to 0} g_0(\lambda) = 1$. In this limit, the term with $l = 0$ becomes dominant, and thus the only non-zero multipole coefficient σ_{lm} is that with $l = m = 0$. There, $\lim_{\lambda\to 0} \sigma_{00} = \sqrt{4\pi} Q$, with $Q = \sum_k q_k$ the total charge on the sphere. Inserting this into the expression for the multipole expansion of the surface charge density, Eq. (5), we get indeed that

$$\lim_{\lambda\to 0} \sigma(\Omega) = \frac{Q e_0}{4\pi R^2}, \quad \text{(D2)}$$

a uniform distribution on a sphere.

In the other limit where $\lambda \to \infty$, the function $g_l(\lambda)$ always tends to 1, independent of l:

$$\lim_{\lambda\to\infty} g(l,\lambda) = 1 \quad \forall l. \quad \text{(D3)}$$

The multipole coefficients σ_{lm} simplify to $\lim_{\lambda\to\infty} \sigma_{lm} = 4\pi \sum_k q_k Y_{lm}^*(\Omega_k)$, yielding

$$\lim_{\lambda\to\infty} \sigma(\Omega) = \frac{e_0}{R^2} \sum_k q_k \sum_{l,m} Y_{lm}^*(\Omega_k) Y_{lm}(\Omega)$$
$$= \frac{e_0}{R^2} \sum_k q_k \, \delta(\Omega - \Omega_k), \quad \text{(D4)}$$

which is indeed a surface charge distribution composed of Dirac δ functions centered at Ω_k. Here we also see why, when using Dirac δ functions for the description of point

charges, in principle an infinite sum over ℓ is needed to represent the distribution correctly.

As for the multipole magnitudes, the only non-zero moment in the limit of $\lambda \to 0$ is of course S_0, with all higher multipoles tending to zero, $\lim_{\lambda\to 0} S_l/|S_0| = 0$ for $l \geqslant 1$. On the other hand, the multipole magnitudes in the limit of $\lambda \to \infty$ are determined purely by their geometrical factor

$$\lim_{\lambda\to\infty} \frac{S_l}{|S_0|} = \frac{S_l^\infty}{|S_0|} = \sqrt{\frac{1}{N} + \frac{2}{N^2} \sum_{k>t} P_l(\cos\gamma_{kt})}, \quad \text{(D5)}$$

which is dependent on the spherical distances between the charges on the sphere, $\cos\gamma_{kt}$.

Appendix E: Additional figures

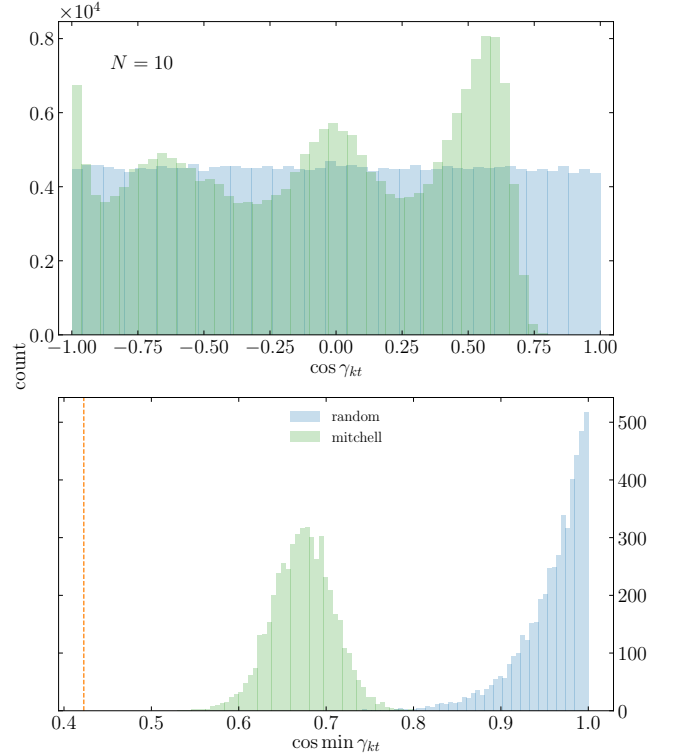Here, we show several additional figures complementing the results presented in the main text.

Figure 8. Histogram of distances between charges, given by $\cos\gamma_{kt}$, and of the closest distance between two charges, $\cos\min\gamma_{kt}$ with $k \neq t$. The histograms were obtained from 5000 different random and Mitchell configurations of $N = 10$ identical charges. The dashed vertical line shows the minimum distance of the corresponding Thomson configuration.
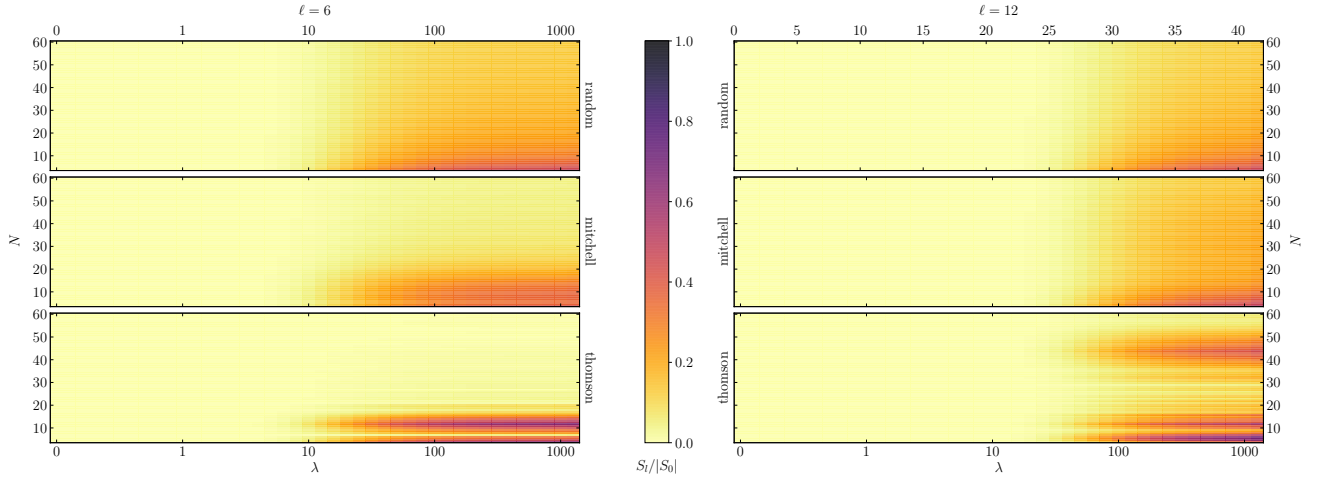
Figure 11. Heatmaps of normalized multipole magnitudes $S_l/|S_0|$ as a function of λ and N for two different values of $\ell = 6$, 12. In the case of random and Mitchell configurations, the heatmaps show the mean values obtained by averaging over 5000 different configurations. The last columns of the heatmaps show the values of the multipole magnitudes in the limit $\lambda \to \infty$, $S_l^\infty/|S_0|$.
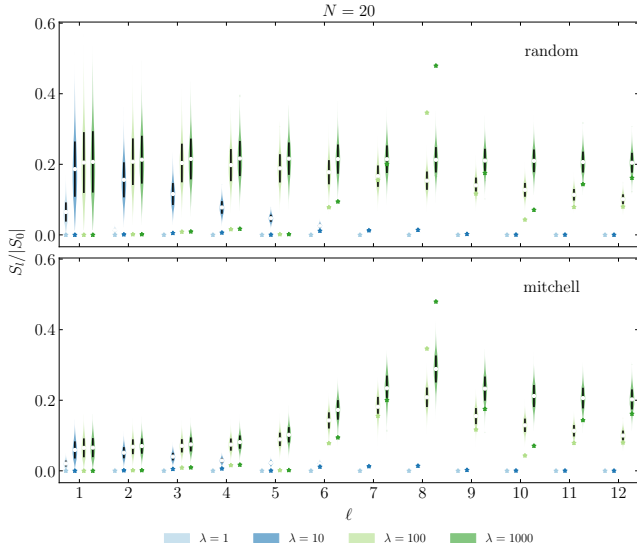

Figure 9. Violin plot of the first 12 multipole magnitudes for configurations of $N = 20$ identical charges, generated either randomly or by using Mitchell's algorithm. Each entry in the violin plot shows a (mirrored) distribution of normalized magnitudes of 5000 different configurations, with the central symbols denoting the mean and the bars denoting the corresponding standard deviation. Star symbols show the multipole magnitudes of the corresponding Thomson configuration. The plot is shown for four different values of the concentration parameter λ.
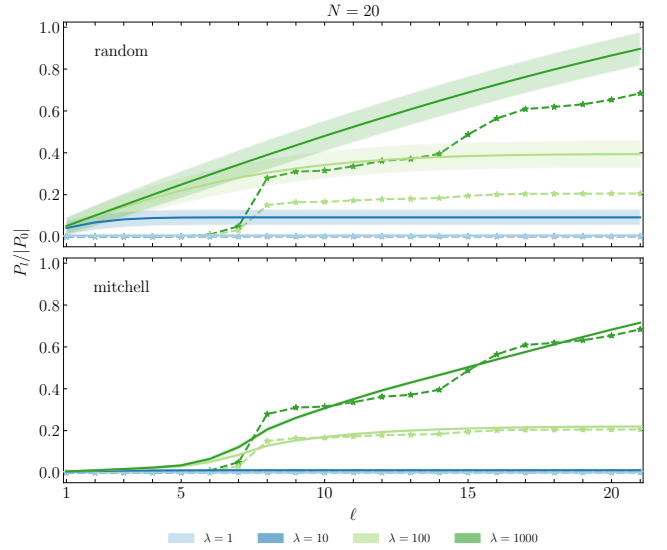
Figure 10. Normalized total power $P_l/|P_0|$ of random and Mitchell configurations of $N = 20$ identical charges, obtained by summing the squares of multipole magnitudes up to order ℓ. Full lines show the mean values, obtained by averaging over 5000 different configurations, while the shaded regions denote the corresponding standard deviations. The latter are negligible for Mitchell configurations. Dashed lines and star symbols show the total power for the corresponding Thomson configuration. The plot is shown for four different values of the concentration parameter λ.

[1] C. Holm, P. Kékicheff, and R. Podgornik, eds., *Electrostatic Effects in Soft Matter and Biophysics*, vol. 46 of *NATO Science Series II – Mathematics, Physics and Chemistry.* Springer, 2012.

[2] E. Bianchi, B. Capone, I. Coluzza, L. Rovigatti, and P. D. J. van Oostrum, *Limiting the valence: advancements and new perspectives on patchy colloids, soft functionalized nanoparticles and biomolecules*, Phys. Chem. Chem. Phys. **19**, 19847–19868 (2017).

[3] E. Bianchi, P. D. van Oostrum, C. N. Likos, and G. Kahl, *Inverse patchy colloids: Synthesis, modeling and self-organization*, Curr. Op. Colloid Interface Sci. **30**, 8–15 (2017).

[4] A. Šiber, A. Lošdorfer Božič, and R. Podgornik, *Energies and pressures in viruses: contribution of nonspecific electrostatic interactions*, Phys. Chem. Chem. Phys. **14**, 3746–3765 (2012).

[5] Y. Bai, Q. Luo, and J. Liu, *Protein self-assembly via supramolecular strategies*, Chem. Soc. Rev. **45**, 2756–2767 (2016).

[6] E. Bianchi, C. N. Likos, and G. Kahl, *Tunable assembly of heterogeneously charged colloids*, Nano Lett. **14**, 3412 (2014).

[7] M. Barisik, S. Atalay, A. Beskok, and S. Qian, *Size dependent surface charge properties of silica nanoparticles*, J. Phys. Chem. C **118**, 1836–1842 (2014).

[8] R. Kusters, H.-K. Lin, R. Zandi, I. Tsvetkova, B. Dragnea, and P. van der Schoot, *Role of charge regulation and size polydispersity in nanoparticle encapsulation by viral coat proteins*, J. Phys. Chem. B **119**, 1869–80 (2015).

[9] M. Sabapathy, R. A. M. K, and E. Mani, *Self-assembly of inverse patchy colloids with tunable patch coverage*, Phys. Chem. Chem. Phys. **19**, 13122–13132 (2017).

[10] A. Lošdorfer Božič and R. Podgornik, *pH dependence of charge multipole moments in proteins*, Biophys. J. **113**, 1454–1465 (2017).

[11] M. Krishnan, *A simple model for electrical charge in globular macromolecules and linear polyelectrolytes in solution*, J. Chem. Phys. **146**, 205101 (2017).

[12] R. J. Nap, A. Lošdorfer Božič, I. Szleifer, and R. Podgornik, *The role of solution conditions in the bacteriophage PP7 capsid charge regulation*, Biophys. J. **107**, 1970–1979 (2014).

[13] A. I. Abrikosov, B. Stenqvist, and M. Lund, *Steering patchy particles using multivalent electrolytes*, Soft Matter (2017).

[14] P. Ni, Z. Wang, X. Ma, N. C. Das, P. Sokol, W. Chiu, B. Dragnea, M. Hagan, and C. C. Kao, *An examination of the electrostatic interactions between the N-terminal tail of the brome mosaic virus coat protein and encapsidated RNAs*, J. Mol. Biol. **419**, 284–300 (2012).

[15] A. Warshel, P. K. Sharma, M. Kato, and W. W. Parson, *Modeling electrostatic effects in proteins*, Biochim. Biophys. Acta Proteins Proteomics **1764**, 1647–1676 (2006).

[16] R. M. Adar, D. Andelman, and H. Diamant, *Electrostatics of patchy surfaces*, Adv. Colloid Interface Sci. **247**, 198–207 (2017).

[17] M. Grant, *Nonuniform charge effects in protein-protein interactions*, J. Phys. Chem. B **105**, 2858–2863 (2001).

[18] A. Lošdorfer Božič and R. Podgornik, *Symmetry effects in electrostatic interactions between two arbitrarily charged shells in the Debye-Hückel approximation*, J. Chem. Phys. **138**, 074902 (2013).

[19] S. Li, G. Erdemci-Tandogan, J. Wagner, P. van der Schoot, and R. Zandi, *Impact of a nonuniform charge distribution on virus assembly*, Phys. Rev. E **96**, 022401 (2017).

[20] W. Li, B. A. Persson, M. Morin, M. A. Behrens, M. Lund, and M. Zackrisson Oskolkova, *Charge-induced patchy attractions between proteins*, J. Phys. Chem. B **119**, 503–508 (2015).

[21] J. F. Vega, E. Vicente-Alique, R. Nez-Ramrez, Y. Wang, and J. Martnez-Salazar, *Evidences of Changes in Surface Electrostatic Charge Distribution during Stabilization of HPV16 Virus-Like Particles*, PLoS ONE **11**, 1–17 (2016).

[22] M. A. Blanco and V. K. Shen, *Effect of the surface charge distribution on the fluid phase behavior of charged colloids and proteins*, J. Chem. Phys. **145**, 155102 (2016).

[23] J. M. Dempster and M. Olvera de la Cruz, *Aggregation of heterogeneously charged colloids*, ACS Nano **10**, 5909–5915 (2016).

[24] C. Yigit, J. Heyda, and J. Dzubiella, *Charged patchy particle models in explicit salt: Ion distributions, electrostatic potentials, and effective interactions*, J. Chem. Phys. **143**, 064904 (2015).

[25] C. Yigit, M. Kanduč, M. Ballauff, and J. Dzubiella, *Interaction of Charged Patchy Protein Models with Like-Charged Polyelectrolyte Brushes*, Langmuir **33**, 417–427 (2017).

[26] G. Silbert, D. Ben-Yaakov, Y. Dror, S. Perkin, N. Kampf, and J. Klein, *Long-Ranged Attraction between Disordered Heterogeneous Surfaces*, Phys. Rev. Lett. **109**, 168305 (2012).

[27] S. Perkin, N. Kampf, and J. Klein, *Long-Range Attraction between Charge-Mosaic Surfaces across Water*, Phys. Rev. Lett. **96**, 038301 (2006).

[28] E. E. Meyer, Q. Lin, T. Hassenkam, E. Oroudjev, and J. N. Israelachvili, *Origin of the long-range attraction between surfactant-coated surfaces*, Proc. Natl. Acad. Sci. USA **102**, 6839–6842 (2005).

[29] T. Hoppe, *A simplified representation of anisotropic charge distributions within proteins*, J. Chem. Phys. **138**, 174110 (2013).

[30] M. Stipsitz, G. Kahl, and E. Bianchi, *Generalized inverse patchy colloid model*, J. Chem. Phys. **143**, 114905 (2015).

[31] C. E. Felder, J. Prilusky, I. Silman, and J. L. Sussman, *A server and database for dipole moments of proteins*, Nucleic Acids Res. **35**, W512–W521 (2007).

[32] H. Nakamura and A. Wada, *Nature of the charge distribution in proteins. III. Electric multipole structures*, J. Phys. Soc. Jpn. **54**, 4047–4052 (1985).

[33] R. Paulini, K. Müller, and F. Diederich, *Orthogonal multipolar interactions in structural chemistry and biology*, Angew. Chem. Int. Ed. **44**, 1788–1805 (2005).

[34] S. Parimal, S. M. Cramer, and S. Garde, *Application of a spherical harmonics expansion approach for calculating ligand density distributions around proteins*,

J. Phys. Chem. B **118**, 13066–13076 (2014).

[35] J. Y. Kim, S. H. Ahn, S. T. Kang, and B. J. Yoon, *Electrophoretic mobility equation for protein with molecular shape and charge multipole effects*, J. Colloid Interface Sci. **299**, 486–492 (2006).

[36] A. Gramada and P. E. Bourne, *Multipolar representation of protein structure*, BMC Bioinformatics **7**, 242 (2006).

[37] V. Lorman and S. Rochal, *Density-wave theory of the capsid structure of small icosahedral viruses*, Phys. Rev. Lett. **98**, 185502 (2007).

[38] V. Lorman and S. Rochal, *Landau theory of crystallization and the capsid structures of small icosahedral viruses*, Phys. Rev. B **77**, 224109 (2008).

[39] A. Lošdorfer Božič, A. Šiber, and R. Podgornik, *Electrostatic self-energy of a partially formed spherical shell in salt solution: Application to stability of tethered and fluid shells as models for viruses and vesicles*, Phys. Rev. E **83**, 041916 (2011).

[40] K. V. Mardia and P. E. Jupp, *Directional statistics*, vol. 494. John Wiley & Sons, 2009.

[41] M. Abramowitz and I. A. Stegun, *Handbook of mathematical functions*, vol. 55. Dover Publications, 1964.

[42] D. P. Mitchell, *Spectrally Optimal Sampling for Distribution Ray Tracing*, SIGGRAPH Comput. Graph. **25**, 157–164 (1991).

[43] D. J. Wales and S. Ulker, *Structure and dynamics of spherical crystals characterized for the Thomson problem*, Phys. Rev. B **74**, 212101 (2006).

[44] J. P. Snyder, *Map projections – A working manual*, vol. 1395. US Government Printing Office, Washington, DC, 1987.

[45] A. Gelessus, W. Thiel, and W. Weber, *Multipoles and symmetry*, J. Chem. Ed. **72**, 505 (1995).

[46] A. Lošdorfer Božič, A. Šiber, and R. Podgornik, *Statistical analysis of sizes and shapes of virus capsids and their resulting elastic properties*, J. Biol. Phys. **39**, 215–228 (2013).

[47] A. Stone, *Distributed multipole analysis, or how to describe a molecular charge distribution*, Chem. Phys. Lett. **83**, 233–239 (1981).

[48] S. Larsson and M. Braga, *Atomic charges based on spherical harmonics expansion at the atomic centers*, Theor. Chim. Acta **68**, 291–300 (1985).

[49] S. Dharmavaram, F. Xie, W. Klug, J. Rudnick, and R. Bruinsma, *Orientational phase transitions and the assembly of viral capsids*, Phys. Rev. E **95**, 062402 (2017).

[50] J. T. Kent, *The Fisher-Bingham distribution on the sphere*, J. R. Stat. Soc. Series B Stat. Methodol. **44**, 71–80 (1982).

[51] G. B. Arfken and H. J. Weber, *Mathematical methods for physicists*. Academic Press, San Diego, CA, 4th ed., 1995.

[52] Wolfram Research Inc., *Mathematica 8.0*, 2010.